**Self-sensing cementitious composites with hierarchical carbon fiber-carbon nanotube composite fillers for crack development monitoring of a maglev girder**

*Siqi Ding, Xinyue Wang, Liangsheng Qiu, Yi-Qing Ni, Xufeng Dong, Yanbin Cui, Ashraf Ashour, Baoguo Han * and Jinping Ou*

Dr. Siqi Ding, Prof. Jinping Ou
School of Civil and Environmental Engineering, Harbin Institute of Technology, Shenzhen, Shenzhen 518055, China

Dr. Xinyue Wang, Mr. Liangsheng Qiu, Prof. Baoguo Han
School of Civil Engineering, Dalian University of Technology, Dalian 116024, China
E-mail: hanbaoguo@dlut.edu.cn, hithanbaoguo@163.com

Prof. Yi-Qing Ni
Department of Civil and Environmental Engineering, The Hong Kong Polytechnic University, Hung Hom, Kowloon, Hong Kong, China

Prof. Xufeng Dong
School of Materials Science and Engineering, Dalian University of Technology, Dalian 116024, China

Prof. Yanbin Cui
Institute of Process Engineering, Chinese Academy of Sciences, Beijing 100190, China

Prof. Ashraf Ashour
Faculty of Engineering & Informatics, University of Bradford, Bradford BD7 1DP, UK

Keywords: (self-sensing cementitious composites, carbon nanotubes, carbon fibers, in-situ synthesis, crack/damage monitoring of maglev girder)

In view of high-performance, multifunctional and low-carbon development of infrastructures, there is a growing demand for smart engineering materials, making infrastructures intelligent. This paper reports a new-generation self-sensing cementitious composite (SSCC)

incorporated with a hierarchically structured carbon fiber-carbon nanotube composite filler (CF-CNT), which is in-situ synthesized by directly growing CNT on CF. Various important factors including catalyst, temperature, and gas composition are considered to investigate their kinetic and thermodynamic influence on CF-CNT synthesis. The reciprocal architecture of CF-CNT not only alleviates the CNT aggregation, but also significantly improves the interfacial bonding between CF-CNTs and matrix. Due to the synergic and spatially morphological effects of CF-CNT, i.e., the formation of widely distributed multiscale reinforcement networks, SSCCs with CF-CNTs exhibit high mechanical properties and electrical conductivity as well as excellent self-sensing performances, particularly enhanced sensing repeatability. Moreover, the SSCCs with CF-CNTs are integrated into a full-scale maglev girder to devise a smart system for crack development monitoring. The system demonstrates high sensitivity and fidelity to capture the initiation of cracks/damage, as well as progressive and sudden damage events until complete failure of the maglev girder, indicating its considerable potential for structural health monitoring of infrastructures.

## 1. Introduction

Deterioration and ageing of infrastructures under environmental actions require reliable structural health monitoring that allows damage to be detected in advance, with the goals of improving their safety and resilience, lowering their maintenance costs, preventing their catastrophic failure, and extending their service life, hence indirectly minimizing their environmental footprint. Until recently, traditional structural health monitoring techniques, mainly including laborious visual inspections, expensive acoustic emission-based, ultrasonic-based, electromagnetic-based techniques, and delicate optical fiber sensing techniques have shown poor long-term durability and compatibility with infrastructures that are mostly made of cementitious composites. [1–5] With the rapid advances of new infrastructures such as high-rise buildings, high-speed rail, floating structures, and maglev, the demand for new-generation structural health monitoring technology to complement the present bottleneck of diagnostics and evaluation of structural conditions and constructing smart infrastructures is therefore increasing. Mimicking human behavior, self-sensing cementitious composite (SSCC), incorporated with conductive fillers as neural networks can directly transduce mechanical or physical stimulations and its own internal condition into recognizable electronic signals without any extrinsic sensing elements. Owing to its intrinsic cementitious nature, SSCC features inherent host compatibility and an identical lifespan with infrastructures, being

considered as an important paradigm for updating infrastructures with smart digital insights.[6–11] To date, broad engineering applications of SSCCs for smart infrastructure monitoring have been explored, such as earthquake-induced damage detection and localization in masonry structures,[12] structural modal identification and health monitoring of five-story building structures,[13] crack detection in concrete beams,[14] chloride penetration monitoring in reinforced mortar,[15] and high-speed rail infrastructure monitoring.[16]

Studies so far have shown that the sensing performance of SSCC is determined by the conductive fillers.[6,7] Due to its excellent mechanical properties, high chemical stability in aggressive environments, high temperature resistance, environment friendly, and more importantly, high electrical conductivity, carbon fiber (CF) has been most extensively employed as conductive filler for manufacturing SSCCs since the pioneering work reported by Chung et al. in the early 1990s.[17] Many studies have reported its excellent performance in reducing SSCC's electrical resistivity by several orders of magnitude and achieving moderate gauge factor in a range of tens to hundreds, dependent on the concentration and aspect ratio of CF.[18–20] However, owing to the poor bonding between smooth CF and cement matrix and the fiber push-in and pull-out sensing mechanism, SSCCs functionalized with CF have exhibited poor self-sensing repeatability upon repeated loading.[17,21] In addition, the CF content near or beyond the percolation threshold (typically 1.5 vol.% or above) is always required to achieve an acceptable level of self-sensing sensitivity, which may lead to structural instability and severely compromise its reinforcement effect on mechanical properties of SSCCs, even considerable structural degradation.[22,23]

To address this challenge, CF surface specifically treated via oxidation, [24–26] or coatings may substantially enhance the bond strength with the cementitious matrix.[27–30] Besides, introduction of a hybrid of CF and other conductive fillers such as steel fiber,[31,32] carbon black,[33,34] carbon nanofiber (CNF),[35,36] carbon nanotube (CNT),[15,37] and graphene[38] to form a hierarchical conductive network could further improve the SSCC's sensing linearity, stability and repeatability due to their synergic effect. In particular, the combination of CF and CNT acts as a ground-breaking attempt to fabricate SSCC with combined superior mechanical, electrical, and self-sensing properties due to the extraordinary mechanical properties, extremely high aspect ratio, and superior electrical conductivity of CNTs.[39,40] For example, Azhari et al reported that the addition of 1 wt.% CNT and 15 wt.% CF could very well increase the accuracy and repeatability of SSCC with an error margin of only $\pm 0.02$,

much lower than the case of 15 wt.% CF alone (±0.08).[37] However, dispersing CNTs uniformly throughout the cement matrix represents a critical challenge for retaining CNT reinforcement efficiency.[41,42] Despite advances in the dispersion techniques of CNTs in the cement matrix, such as covalent and non-covalent functionalization and ultrasonication, have been made, these complicated and multi-step dispersion methods restrict CNT's large-scale applications in construction industry.[43]

With advances in nano-synthetic and nanocomposite technologies, the recent trend has been focused on in situ-growth of CNTs or ex situ-grafting CNTs on the CF surface to create an all-carbon hierarchical composite system (CF-CNT), in which nanoscale CNT reinforcement alongside the CF surface minimizes or eliminates dispersion issues of CNTs by transferring the nanoscale dispersion into the microdomain as well as improving their composite effectiveness and efficiency.[44] Electrophoretic depositions,[45] chemical reactions with functionalized CNTs and CFs,[46] and direct growth of CNTs on CFs via chemical vapor deposition (CVD) techniques have been reported as being efficient routes for manufacturing CF-CNT hierarchical composites.[47] Among these strategies, the CVD route has been widely accepted as one of the most efficient routes for large-scale synthesis of CNTs. Compared with other strategies, growing CNTs on the surface of CF via CVD method has the advantages of one-step synthesis and dispersion, controllable CNT morphology and orientation, numerous tunable CVD parameters, versatile application scenarios, and scalable production.[16,48,49] It is reported that the radial orientation of CNTs on CFs improved the interfacial strength of CF/resin composites by 15-475% and achieved nearly 5% improvement in the flexural modulus of CF/resin composites due to modification of the CF surface.[44] In addition, CF-CNT hierarchical composites led to an increase of in-plane and out-plane electrical conductivities by 330% and 510% over the unmodified CF/epoxy composites,[50] indicating that the CF-CNTs can provide abundantly more conducting paths in the composite, enabling the composite with the self-sensing property to detect crack propagation when employed for structural health monitoring.[51] At present, most investigations have considered the production and characterization of CF-CNT reinforced polymer-based composites, focusing on the mechanical improvements from interlaminar toughness to tensile strength, however, no study has looked at the implications of CF-CNT on mechanical and electrical properties of the resulting cementitious composites, particularly its feasibility for manufacturing SSCCs.

Here, for the first time, we report a new-generation SSCC with high mechanical properties and notable self-sensing performance, fabricated by a multiscale-designed all-carbon CF-CNT composite filler via in-situ CVD method. The complexity of the in-situ CVD growth of the CF-CNT hierarchical fillers was systematically examined by suitably tuning the CVD parameters. As a facile and one-step strategy, the in-situ CVD method enables the scalable production of CF-CNTs with high-density and radially oriented CNT coverage. With the incorporation of optimized CF-CNT hierarchical fillers, the SSCCs exhibited impressive mechanical, electrical and self-sensing properties due to the homogeneous distribution of CNTs in the matrix, the enhanced CF-CNT-cement interfacial bond strength, and the synergic and spatially morphological effects of CF-CNT. The SSCCs can also perform real-time crack development monitoring of a real maglev girder, thus providing the most fundamental materials for energizing sustainable infrastructures with integrated digital insights.

## 2. Results and Discussion

### 2.1. Synthesis and structural characterization of CF-CNTs

The synthesis process of CF-CNTs, including CF surface oxidation, catalyst impregnation, and CVD growth, is schematically illustrated in **Figure 1**a. Unsized polyacrylonitrile (PAN)-based short-cut CFs were used as substrates (see Table S1 for the main physical properties of CFs). Before catalyst deposition, CF surfaces were modified using the liquid-phase oxidation method to promote their wettability and help stabilize the catalyst particles.[52] Figure S1 shows cleaner CF surfaces after acid oxidation than the as-received CFs. For the catalyst impregnation, the oxidized CFs were immersed into the catalyst precursor isopropanol solution for 2 h along with the assistance of ultrasonic treatment. Subsequently, the catalyst pre-deposited CFs were filtered from the solution and oven-dried at 80 ºC for 24 h. The growth of CNTs was performed in an ambient pressure CVD system using $C_2H_2$ as carbon source. Two types of transition metals including iron and nickel were used as catalysts under a CVD regime of $C_2H_2/H_2/N_2$ (20/20/100 sccm), at 650 ºC for 30 min. Figure 1 shows the SEM images of CF-CNTs architectures length evolutions of CNTs on CFs as a function of growth time with different types of catalysts. Before CVD process, the CF surface was loaded with uniform and nanosized catalyst particles when iron was the catalyst (Figure 1b) due to the ultrasonic treatment during the catalyst deposition process (Figure S2).

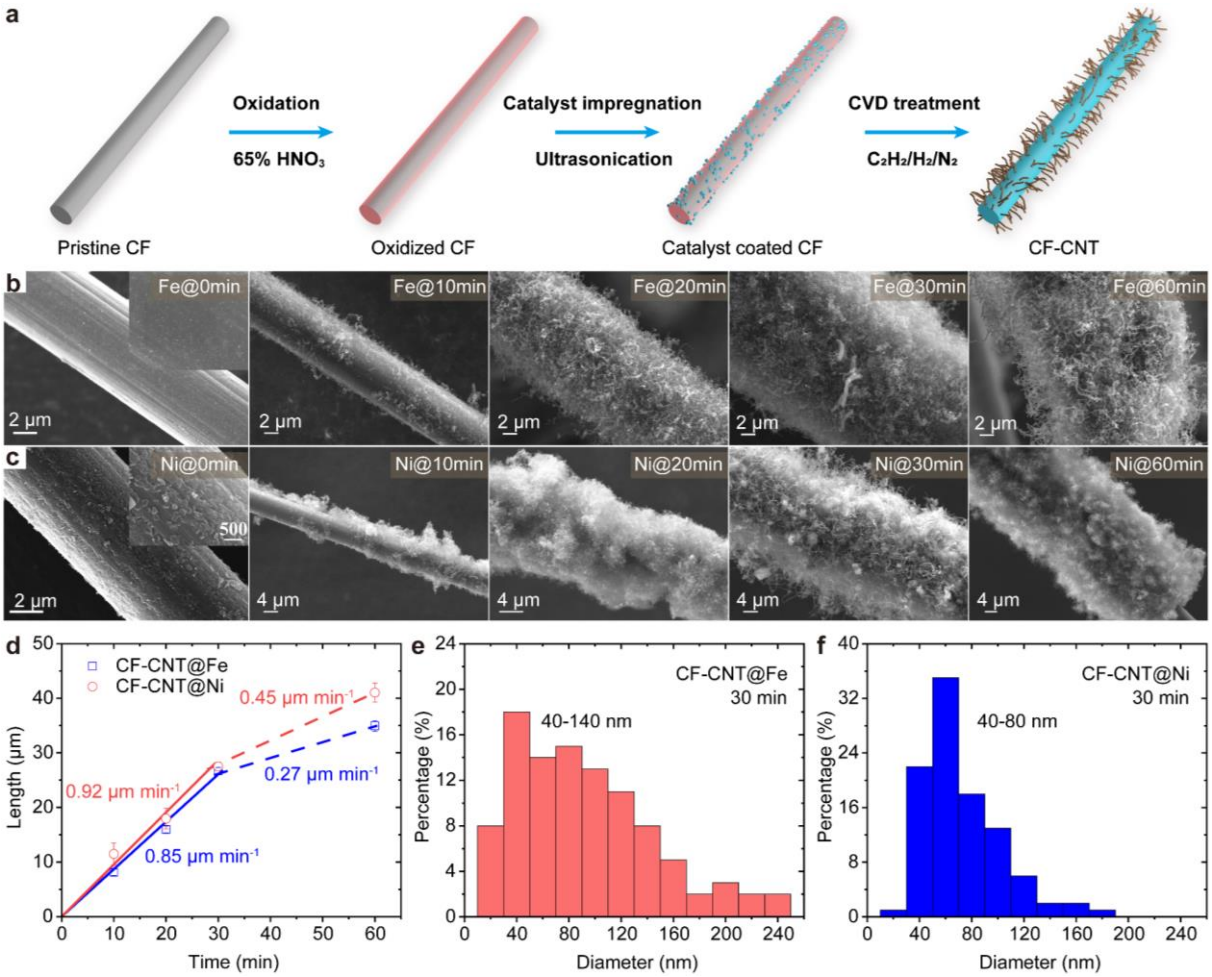


**Figure 1.** Synthesis of CF-CNTs via CVD method. (a) Schematic illustration of the synthesis process. (b) Morphology evolution of CF-CNTs with different growth times from 0-60 min using $Fe(NO_3)_3 \cdot 9H_2O$ as catalyst. (c) Morphology evolution of CF-CNTs with different growth times from 0-60 min using $Ni(NO_3)_2 \cdot 6H_2O$ as catalyst. (d) Length evolutions of CF-CNT@Fe and CF-CNT@Ni as a function of growth time, the values labelled correspond to the slopes of linear fitted lines. (e) Diameter distribution of CF-CNT@Fe. (f) Diameter distribution of CF-CNT@Ni. (Growth condition: $C_2H_2/H_2/N_2$=20/20/100 sccm, 650 ºC, 30 min).

For using nickel as catalyst, the catalyst particles had cellular structures with larger size distribution and higher loading density than the iron catalyst (Figure 1c). After the CVD process, both were efficient in catalyzing $C_2H_2$ for CNT growth. However, an improvement of the CNT quality was observed on CFs in the case of nickel catalyst. The CNT length in the case of nickel catalyst was also several times longer than using iron catalyst, consistent with the previous result that the catalytic efficiency of iron was much less than that of nickel at 650 ºC.[53] In addition, the CF surface was covered by a layer of sparse CNT "embryos" with a

substantial percentage of surface area uncovered when the growth time was 10 min for the case of iron catalyst, which provides the sites for subsequent CNT growth. In comparison with the iron catalyst, more CNT growth appeared for the nickel catalyst, which further elucidates the higher catalytic activity of nickel at 650 ºC. Uniform coverage can be achieved for both cases at 20 min. When the growth time reached 60 min, CNTs were grown perpendicularly to the CF axis and formed a radial-aligned orientation with a length of more than 30 μm. Using piece-wise linear regression, the growth rates for the nickel and iron catalysts during the first 30 min were estimated to be 0.92 μm $min^{-1}$ and 0.85 μm $min^{-1}$, respectively, but, slowed down to 0.45 μm $min^{-1}$ and 0.27 μm $min^{-1}$, respectively, during the following 30 min (Figure 1d). The outer diameter of the CNTs grown with iron catalyst had a wide distribution of 40-140 nm, whereas a narrower distribution of 40-80 nm was found regarding the outer diameter of the CNTs grown with nickel catalyst, indicating that the nickel catalyst allows the formation of CF-CNTs with more uniform morphology and higher growth rate than the iron catalyst (Figure 1e, f).

**Figure 2**a, b show the SEM images of CF-CNTs grown under various temperatures from 450 °C to 850 °C using $Fe(NO_3)_3 \cdot 9H_2O$ and $Ni(NO_3)_2 \cdot 6H_2O$ isopropanol solutions as catalyst precursors and under $C_2H_2/H_2/N_2$ (20/20/100 sccm) for 30 min. With using iron as the catalyst at 450 °C, no CNT growth appeared on the CF surface (Figure 2a) since the temperature was so low for the diffusion of the pyrolytic carbon atoms into the iron catalyst particles and gradually accumulated on the surface of the CFs. When the temperature rose to 550 °C, the increase in the diffusion of the pyrolytic carbon atoms effectively reduced the accumulation of carbon atoms to grow CNTs. However, the diffusion rate was small at low temperatures, resulting in a low growth rate of CNTs at equilibrium. At the same time, the concentration of pyrolysis carbon atoms landing on the catalyst cracking surface was high and it is easy to cause the local concentration of pyrolysis carbon atoms saturated, thus forming amorphous carbon and causing the catalyst to become deactivated through encapsulation, as observed from that low yield CNTs corresponding with large amounts of amorphous carbons were formed.[54] With the increase of temperature to 650 °C, more obvious CNT growth was observed all over the CF surface. At 750 °C, both the diameter and the length of CNTs dramatically increased, indicating the catalyst is highly efficient and durable at this critical temperature. When the temperature was increased to 850 °C, the CF surface was seriously damaged due to the interaction of the fiber with the catalyst. Fe-C impurities and a few bundles of straight CNTs were observed in Figure 2a. At this point, the interaction between

catalyst and CF became so pronounced that some diffusion paths inside the catalyst particles became blocked, resulting in a decrease in the CNT precipitation rate. While the decomposition of carbon sources was more significant at higher temperatures, the catalyst was deactivated because of amorphous carbon accumulations. When using nickel as the catalyst, irregularly distributed and curled CNTs can be observed on the CF surface even if the temperature was as low as 450 °C (Figure 2b), indicating that the catalytic activity of nickel was much higher than iron at low temperature. This is primarily related to the higher capacity for carbon diffusing in nickel than in iron. Therefore, nickel as the catalyst effectively produced CNTs on the CF surface by the diffusion of pyrolytic carbon atoms at low temperature. Similarly, with increase of temperature, the yield and quality of CNTs were significantly enhanced, showing a positive relationship until 850 °C. The optimal growth temperature range was found to be 650-750 °C for the nickel catalyst. At a temperature exceeding 850 °C, obvious damage to the CF surface also appeared and the yield of CNTs was significantly decreased. Conclusively, the most acceptable temperature range for the CF-CNTs growth was achieved between 550-650 °C.

To investigate the effect of gas composition on CF-CNTs growth, the feed rates of $C_2H_2/H_2/N_2$ were selected at 5/5/100 sccm and 40/40/100 sccm. As shown in Figure 2c, reducing the feed rates of $C_2H_2$ and $H_2$ resulted in a decrease in the yield as well as the CNT average diameter, indicating that a sufficient supply of carbon source is required to fulfill the initial nucleation requirement that determines the diameter of CNTs.[55] However, as shown in Figure 2d, if excessive amounts of $C_2H_2$ and $H_2$ were supplied, the formation of CNTs was blocked because of amorphous carbon accumulation, in particular at 750 ºC, resulting in a significant decline in CNT formation. Of interest, at a high $C_2H_2$ and $H_2$ flow rate, a uniform CNT coverage can be found on CF surface at a temperature as low as 550 ºC, but almost no CNT was formed in the other two cases. Figure 2e summarizes the lengths and diameters of CF-CNT@Fe grown under different gas compositions as a function of growth temperature. It can be seen that the regularity of CNTs growth as a function of temperature was consistent with the results observed above. Therefore, the optimal feed rate of $C_2H_2/H_2/N_2$ was suggested as 20/20/100 sccm in this study.

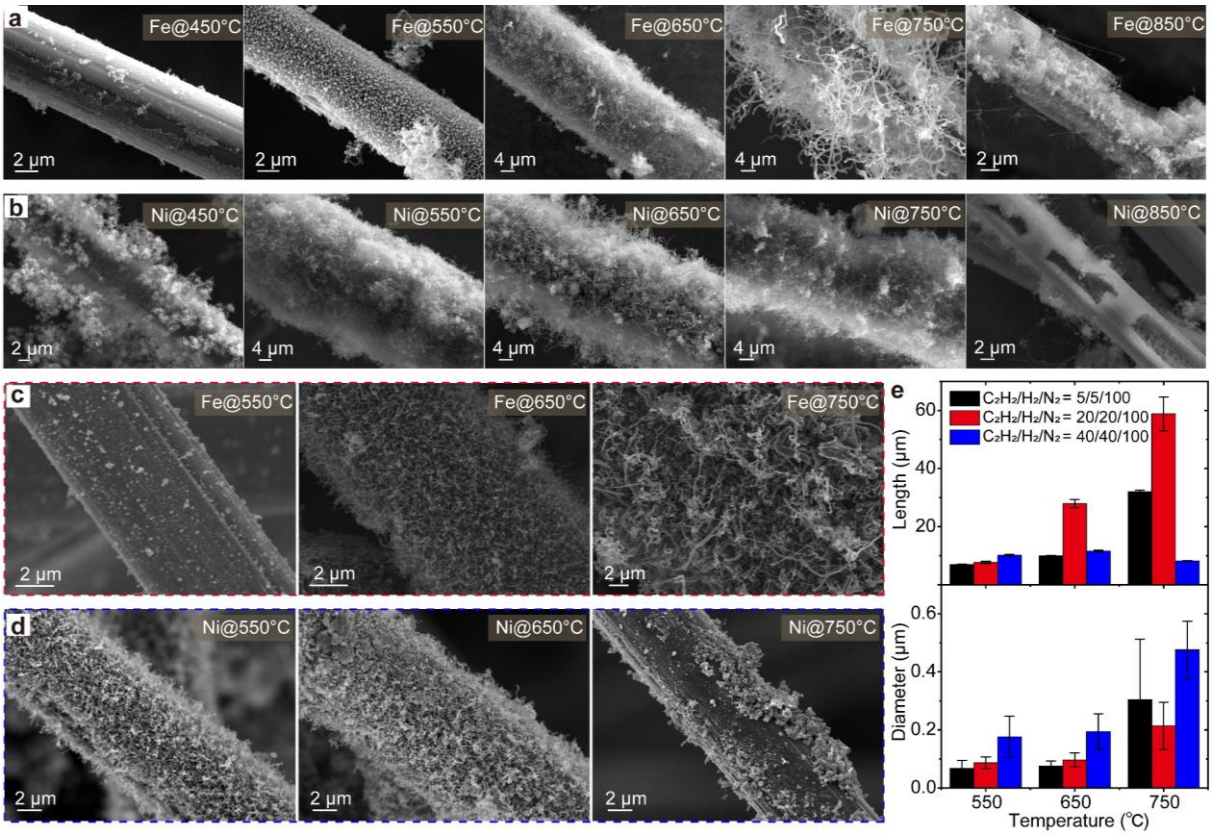


**Figure 2.** Effects of temperature and gas composition on morphologies of CF-CNTs. (a) SEM images of CF-CNTs with different temperatures using $Fe(NO_3)_3 \cdot 9H_2O$ as catalyst. (b) SEM images of CF-CNTs with different temperatures using $Ni(NO_3)_2 \cdot 6H_2O$ as catalyst. (c) SEM images of CF-CNT@Fe grown under a condition of $C_2H_2/H_2/N_2$=5/5/100 sccm, 650 ºC, 30 min. (d) SEM images of CF-CNT@Fe grown under a condition of $C_2H_2/H_2/N_2$=40/40/100 sccm, 650 ºC, 30 min. (e) Comparison on the lengths and diameters of CF-CNT@Fe under different gas compositions.

The above results demonstrate that highly customized CF-CNTs can be successfully achieved by modulating the CVD growth conditions, allowing the utilization of this hierarchically structured filler towards the fabrication of multifunctional cementitious composites. Based on a criterion of growing CNTs with high density and long length, a batch of CF-CNTs was afterward produced using $Ni(NO_3)_2 \cdot 6H_2O$ as catalyst with an optimized CVD regime ($C_2H_2/H_2/N_2$ = 20/20/100 sccm, 650 °C, 30 min), to investigate its effectiveness and efficiency in tailoring SSCCs' performance. As shown in **Figure 3**a, high-density CNTs were uniformly covered on the whole CF surface under the optimized production regime, with an average length of 16.50 μm (the value has subtracted the diameter of CF, i.e., 7 μm), consistent with the results revealed above. The diameter of the as-grown CNTs was estimated to be within 38-74 nm, by counting more than 200 CNTs (Figure 3b). The value was further

verified from TEM images, in which tubular and curly structure of multi-walled CNTs with a diameter of 58 nm were observed (Figure 3c and Figure 3d). Nickel nanoparticles were attached on CNT tips, suggesting the tip-based growth mechanism of CNTs on CFs. The inset of Figure 3d confirms the formation of multi-walled CNTs with a lattice spacing of 0.34 nm, consistent with the graphite's (002) plane. The broad D and G bands at around 1350 $cm^{-1}$ and 1580 $cm^{-1}$ in the Raman spectrum of pristine CF and a high $I_D/I_G$ value of 1.14 indicated its low level of crystallinity and a low-ordered structure (Figure 3e). In contrast, more obvious and sharper D and G bands can be observed at 1336 $cm^{-1}$ and 1590 $cm^{-1}$ respectively after the coverage of CNTs. The $I_D/I_G$ value of 0.93 indicated a reasonable quality but a poorly crystallized CNT structure, in agreement with the TEM observation. This may be mainly attributed to the low CVD temperature. Similarly, the graphite peak at $2\theta = 26^{\circ}$ (indexed as C (002)) of the XRD patterns of CF-CNTs corresponding to the inter-planar spacing of 0.34 nm clearly appeared (Figure 3f). Several peaks indexed to CNT (C (100) plane) at 42.4º and CNT (C (001) plane) at 44.7º (COD 901270) were also observed while there is no significant peak observed in the case of CFs, which further indicates the structural integrity of the as-grown CNTs. TG-DTG analysis was performed under an air atmosphere as shown in Figure 3g, revealing that the two carbon materials performed good thermal stability with no obvious mass loss occurring below 500 ºC. The DTG curve of the CF-CNT exhibited two sharp peaks of weight loss at around 560 ºC and 609 ºC, attributed to the decompositions of CNT and CF, respectively. However, only one peak was observed at 609 ºC for the CF sample, associated with the oxidation of CF. It is therefore assumed that the pronounced weight loss near 560 ºC involved the complete oxidation of CNTs to gaseous products. From the DTG curve, the mass fraction of CNTs in the CF-CNTs can be estimated as 41.92% (see Figure S3), demonstrating the high density and coverage of the synthesized CNTs on CFs. The CF-CNT displayed a hierarchical porous structure and a BET specific surface area of 14.1359 $m^2 g^{-1}$, which is nearly 100 times higher than that for the pristine CF (0.1545 $m^2 g^{-1}$) due to its non-porous or microporous structure (Figure 3h) and smooth surface. The total pore volume of the CF at the pore size range 2-50 nm was only 0.000226 $cm^3 g^{-1}$. In addition, a large number of mesopores with sizes of 2-50 nm was available to the CF-CNTs (Figure S4). The total pore volume of the CF-CNT at the pore size range 2-50 nm was 0.059272 $cm^3 g^{-1}$. This enhanced pore volume is assumed from the CNT interspaces, which would be beneficial in sufficiently immersing the cement matrix region surrounding the CF to ultimately provide a stronger interfacial bonding between the CF-CNTs and cement matrix.

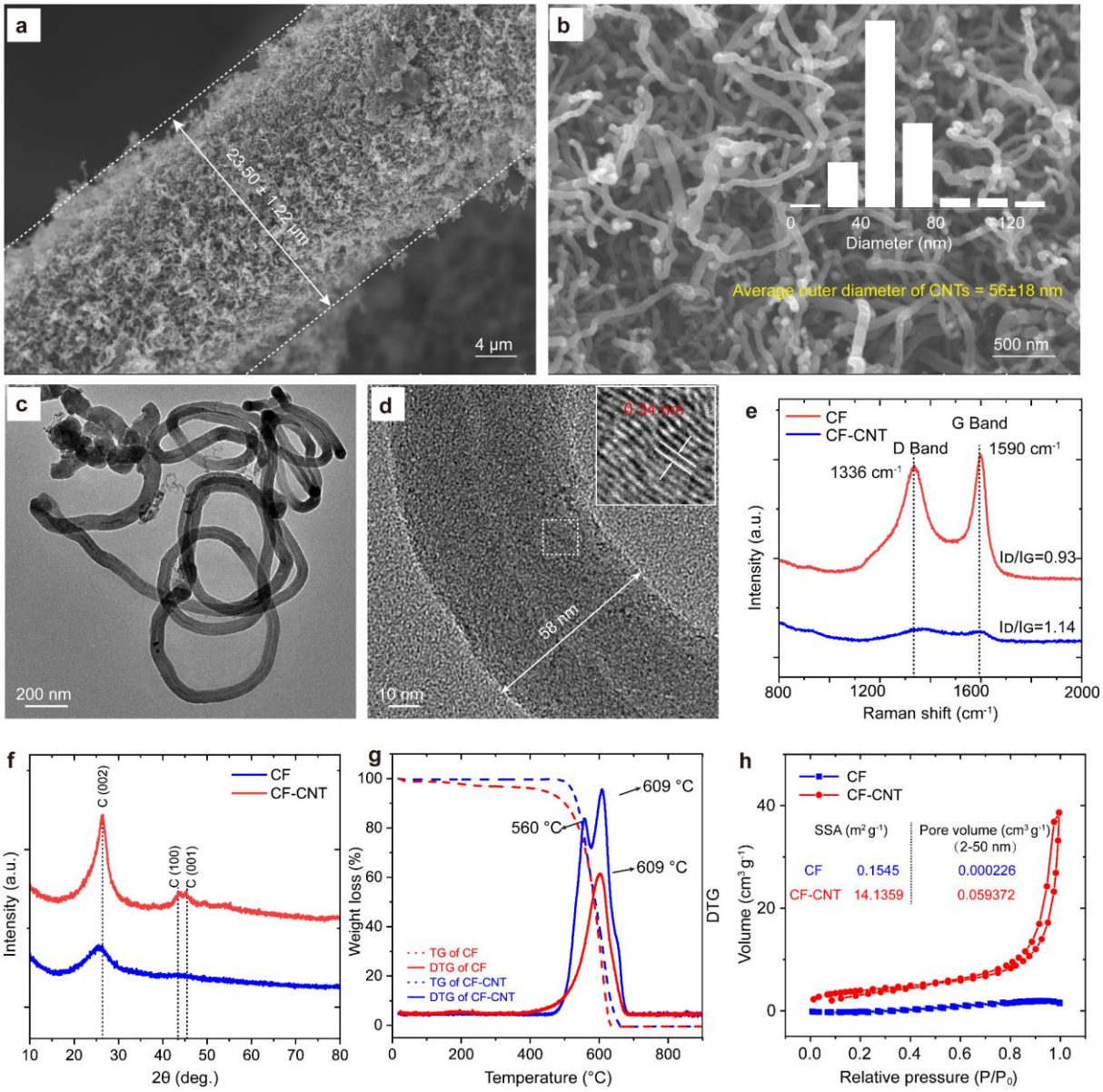


**Figure 3.** Morphology and structure characterization of CF-CNTs. (a) SEM image of CF-CNTs. (b) High-magnification SEM image of CF-CNTs. Inset shows the diameter distribution. (c) TEM image of CF-CNTs. (d) High-resolution TEM images of individual CNT. Inset shows the spacing between two neighboring lattice fringes. (e) Raman spectra. (f) XRD spectra of CFs and CF-CNTs. (g) TG-DTG curves of CFs and CF-CNTs under an air atmosphere. (h) $N_2$ adsorption isotherms, corresponding BET specific surface area and pore volume (ranging from 2 nm to 50 nm) of CFs and CF-CNTs. (Growth condition: $C_2H_2/H_2/N_2$=20/20/100 sccm, 650 ºC, 30 min).

## 2.2. Mechanical properties and microstructures of SSCCs with CF-CNTs

SSCCs with CF-CNTs were fabricated according to the mixture proportions presented in Table S2. The flexural strengths of SSCCs with different CF-CNT contents were investigated in comparison with SSCCs with CFs. As shown in **Figure 4**a, the load-deflection curves exhibited sharp reductions after reaching the ultimate load, indicating typical brittle fracture behavior of SSCCs with CFs and SSCCs with CF-CNTs due to the brittle feature of CFs, which is also evidenced by the failure cracks emerging at mid-span of SSCC specimens (Figure 4b, inset). Previous studies have verified that the addition of CFs and CNTs can both effectively improve the flexural properties of cementitious composites as the fibrous and strong filler can improve the cracking resistance and toughness of cementitious composites by retarding the expansion of flaws in the continuity of the materials, inhibiting the coalescence of microcracks as well as providing a bridging and pull-out effect to delay cracks rapidly opening.[56,57] As expected, the incorporation of CF-CNTs and CFs into cement paste significantly increased the flexural strength compared with that of the plain cement paste. In contrast, the SSCCs with CFs always exhibited higher improvements in flexural properties than SSCCs with CF-CNTs at the same filler content (Figure 4b). The flexural strengths of all SSCCs showed maxima at 2.0 vol.% CFs with 15.526 MPa/282.0% increase, which are much higher than the SSCCs with 2.0 vol.% CF-CNTs that had the highest flexural strength (4.792 MPa/87.1% increase) in the cases of CF-CNTs reinforcement. In addition, these improvements were directly proportional to the filler content. The relatively weak reinforcement effect of CF-CNTs in comparison with CFs may be explained by the deterioration of CF, including surface flaws after thermal degradation, surface oxidation, and internal damages during the harsh growth conditions of CVD processing.[58] Such degraded properties, especially the tensile strength of CFs inevitably sacrifices the properties of hierarchical CF-CNTs, thus mitigating their effective reinforcement in flexural properties of SSCCs.

In terms of compression characterization, as shown in Figure 4c and Figure S5, the compressive strengths of SSCCs with CFs and CF-CNTs both showed an initial increasing trend, followed by a continued decrease with the increase of filler contents. This result can be ascribed to the poor workability of cement paste and poor dispersion of CFs at high filler content, leading to increases in porosity.[26,59,60] However, except for SSCC with 5 vol.% of CFs, all SSCCs incorporated with fibrous fillers displayed higher compressive strengths than the plain specimen. The compressive strengths of SSCCs with CFs showed maxima at 1.0

vol.% CFs with 34.13 MPa/30.87 % increase. In the case of SSCCs with CF-CNTs, the samples with 2.0 vol.% CF-CNTs exhibited the highest increase of compressive strength up to 38.74 MPa/35.03%, even higher than SSCCs with 2.0 vol.% CFs. Meanwhile, when the filler content was 2.0 vol.% or above, the enhancement effect of CF-CNTs on compressive strength of SSCCs became more significant than the case for CFs. Similarly, as shown in Figure 4d, Young's modulus of SSCCs with CFs and CF-CNTs, initially increased with filler content due to the restriction of longitudinal cracks, but then decreased. The samples with 3.0 vol.% CFs and 3.0 vol.% CF-CNTs demonstrated the highest Young's modulus at 36.4 GPa and 32.1 GPa, improved by 8.8 GPa/31.85% and 4.5 GPa/16.16%, respectively compared with the blank, indicating the improved compactness of cement matrix after modification with moderate amounts of CFs and CF-CNTs. However, the Young's modulus of SSCC samples with high filler contents of CF-CNT (3.0 vol.% and above) is not generally higher than that of SSCC samples with the same filler content of CF. This performance reversal of CF and CF-CNT may be attributed to the higher porosity of the SSCC sample with CF-CNT due to the dispersion issue at high filler content (the specific surface area of CF-CNT is much higher than CF so that the increasing CF-CNT incorporation in cement paste indicates a higher amount of water absorbed by CNTs), and the loose architecture of the CF-CNT, as evidenced by its higher pore volume (Figure 3h).

To investigate the reinforcing mechanisms of CFs and CF-CNTs, SEM (BSE) images of fracture surfaces of SSCCs with CFs and with CF-CNTs are displayed in **Figure 5**. In the case of SSCC with CFs, it can be observed that CFs were uniformly distributed and randomly oriented in the cement matrix, forming an extensive reinforcing network. CFs can penetrate the cement matrix by interfacial bonding to provide bridging forces, preventing crack generation and propagation. The increase of loading would cause fiber debonding, pull-out and even failure (Figure 5a). Figure 5b shows CF fossil after pull-out, which closely reflects the shape of a CF groove-like surface. The fossil verifies the interfacial bonding between CF and cement matrix.[60,61] However, the bond strength was relatively weak due to the smooth and untreated CF surface. Cracking caused by matrix shrinkage can be found in the fossil. In terms of hydration products, low-density fibrous calcium silicate hydrates (C-S-H) were observed in the interfacial transition zone between CF and cement paste and on CF surfaces (Figure 5c), indicating that the mechanical connection between CF and matrix was weak, limiting the reinforcement effect of the pristine CF on the mechanical performance of SSCC.[62] With the modification of CNT on CF, it is assumed that the CF-matrix bond

strength was enhanced due to the improvement of the ITZ surrounding CF. As shown in Figure 5d, e, there are hydration products on the CF-CNT surface (marked as strong bonding), corresponding to matrix failure. The CF-CNT fossil after pull-out demonstrated a rough morphology with CNT embedded into the surrounding hydration products (Figure 5e). In addition, no crack was found in the fossil, different from that of the CF fossil. It means that CF-CNTs provided higher crack resistance upon fiber pull-out. At the fiber debonding interface, dense C-S-H, CNT pull-out, CNT bridging, and CNT surface wrapped with hydration products can be observed (Figure S6). Comparing Figure 5g and Figure 5h, there is an obvious ITZ observed around the CF-CNT-cement interface, at which a higher amount of carbon element (54.3 wt.%) was detected with respect to the case of the CF-cement interface (50.2 wt.%). Meanwhile, Ca/Si ratios of C-S-H in the CF-cement interface and CF-CNT-cement interface were 1.30 and 1.14, respectively, indicating that CF-CNT can increase the degree of polymerization of C-S-H.[63] These observations provide plausible evidence that CF-CNT can effectively enhance the CF-CNT-cement matrix interfacial bond strength. CNTs grown on CFs can increase the surface area of CFs and act as nucleating sites to encourage part of hydration products penetrating the CNT forests, forming a strong mechanical anchor between CF-CNT and matrix. The nano-sized CNT particles can also fill in porous structures surrounding the CF, leading to the improvement of ITZ microstructure (Figure 5i). In addition to CF reinforcement at macroscale or microscale, CNT can even bridge the nano-scaled cracks and transfer load from CF to itself, thus delaying crack generation and propagation.[47,64–68]

In addition, as shown in Figure S7, the XRD and TG results both revealed that the addition of CF and CF-CNT had no influence on the compositions of SSCCs' hydration products while can promote their hydration degree to some extent as observed by the higher overall TG mass losses than the blank specimen, consistent with previous studies.[26,69] As compared, the CF-CNT performed more positively in the promotion of SSCC's hydration degree over the CF due to the nucleating effect of CNTs, which further elucidates the reinforcing mechanisms of CF-CNTs. However, as noted above, the flexural properties of SSCCs with CF-CNTs were not much superior against SSCCs with CFs. The unfavorable results may be explained by the degraded performance of CF after CVD processing and the high-density CNTs formed on CF surfaces. There are plenty of etch-pits caused by the interactions between catalyst particles and carbon atoms on CF surface (Figure S6). In addition, high-density CNTs may be difficult to be entirely immersed in cement paste and are prone to separate off during the mechanical

mixing, scattering into the ITZ (Figure S8) and matrix (Figure 5d), i.e., generation of CNT agglomerations. Such CNT agglomerations lead to the formation of many defects such as gaps and pores in the ITZ and matrix, thus limiting their effectiveness as reinforcements.[70,71] The high mass fraction of CNTs in the CF-CNT may also cause the dilution effect on the overall mechanical reinforcement of CF-CNT as the reinforcing effect of short CNT is inferior to the long CF.[59]

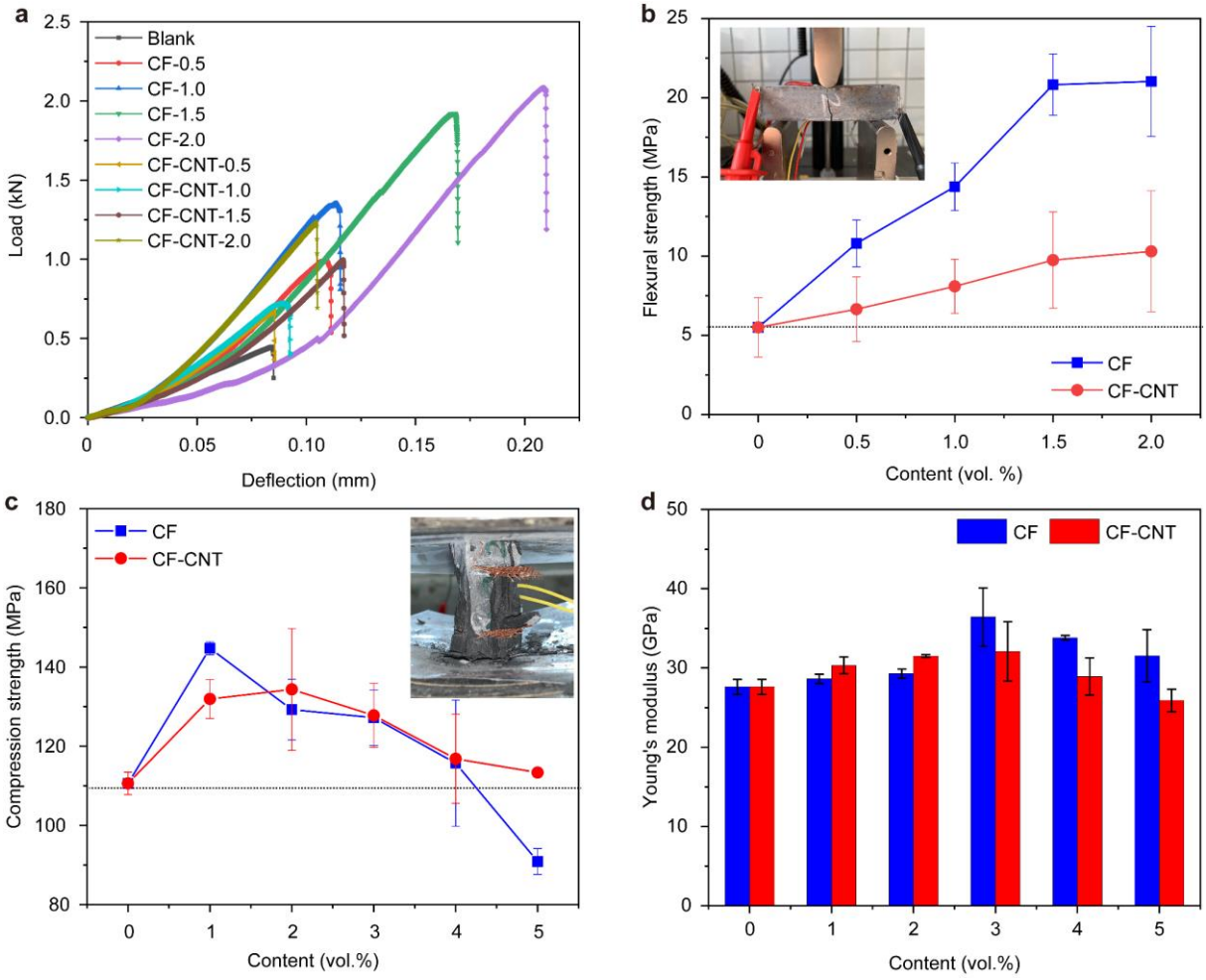


**Figure 4**. Mechanical properties of SSCCs with CFs and CF-CNTs as a function of filler content. (a) Flexural load-deflection curves. (b) Flexural strength (Inset shows a photo of a sample after flexural failure). (c) Compressive strength (Inset shows a photo of a sample after compression failure). (d) Young's modulus of SSCCs with CFs and CF-CNTs under compression.

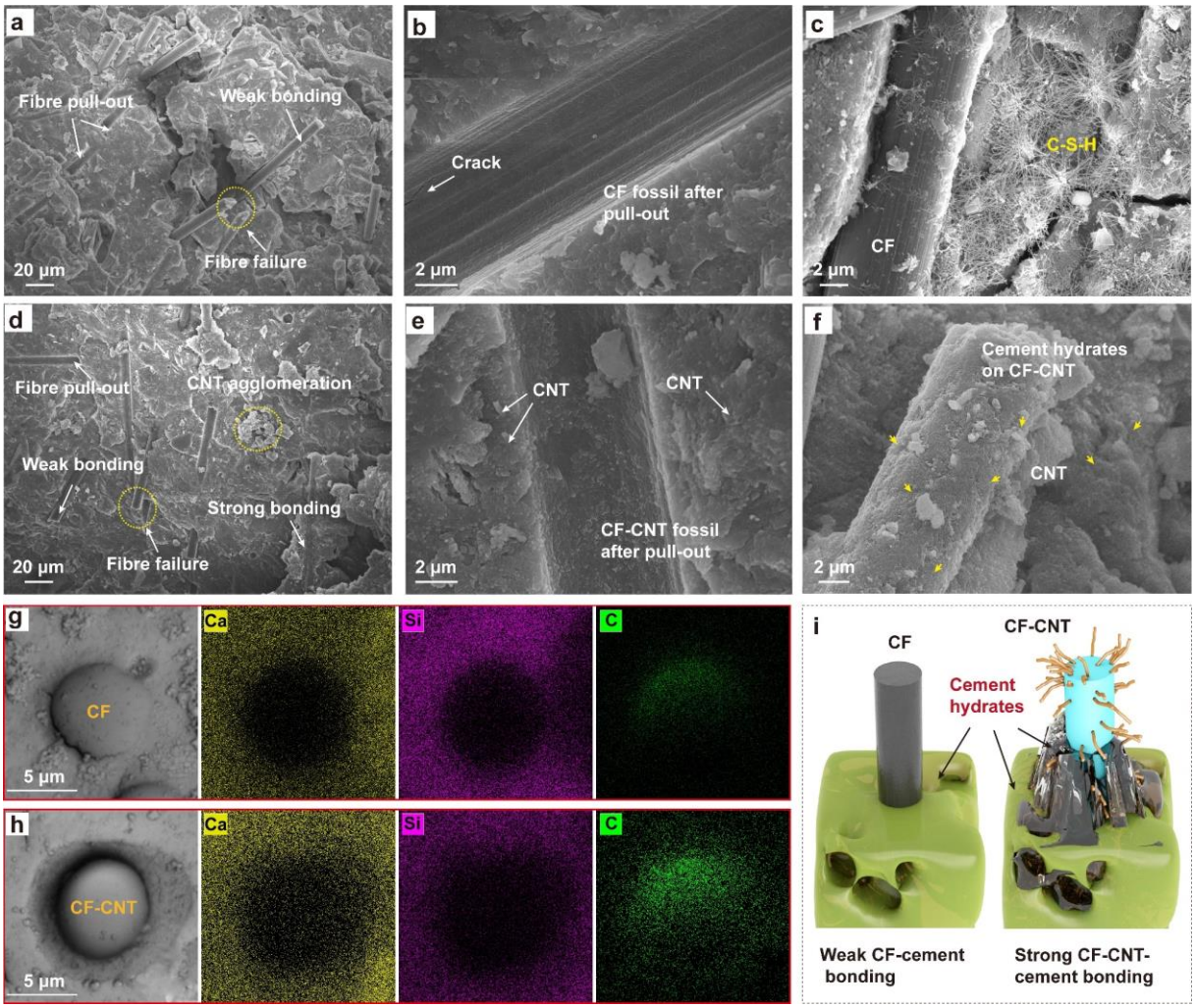


**Figure 5**. Microstructure analysis of SSCCs. (a)-(c) SEM images of CFs. (d)-(f) SEM images of SSCCs with CF-CNTs. (g) BSE image and EDS mappings of the interface between the CF and cement paste. (h) BSE image and EDS mappings of the interface between the CF-CNT and cement paste. (i) Illustration of the reinforcing mechanisms of CF-CNTs after pull-out.

### 2.3. Electrical properties of SSCCs with CF-CNTs

The electrical properties of SSCCs as a function of the filler content were measured using two-probe resistance measurement (Figure 6a). As shown in Figure 6b, the incorporation of 0.5 vol.% of CFs or CF-CNTs alone can considerably decrease the DC electrical resistances of SSCCs. With further increase of filler content, the DC electrical resistance of SSCCs remained almost in the same range as that of 0.5 vol.%. In comparison, the addition of CF-CNTs in SSCCs gained a notable improvement in electrical conductivity compared with the addition of only CFs. However, both CFs and CF-CNTs slightly decreased the DC electrical

resistance of SSCCs by only one order of magnitude. No apparent percolation in which electrical resistance of SSCC is sharply decreased at a certain filler content was observed in this study, even at a high filler content of 5 vol.%. This observation differs from the work reported by Xie et al.,[72] in which percolation can be obtained at only 0.5 vol.% of CFs. However, Chen et al. also found that the conductivity of CF reinforced cementitious composites increased by only one or two orders of magnitude with the addition of 0.5 vol.% CFs.[18] After the CF content reached the percolation threshold (therein, 0.5 vol.%), the conductivity remained unchanged with increase of CF content. Azhari et al. also demonstrated that the electrical resistivity of SSCCs was only reduced by one order of magnitude by adding 7 vol.% of CFs.[73] The percolation phenomena can be observed until CF content becomes as high as 15 vol.%. These findings indicate that SSCC with CFs has a higher percolation threshold than the CNT counterpart (usually lower than 2.0 vol.%),[74] which is attributed to the lower aspect ratio and inherently lower conductivity of CF than CNT.[75]

To further investigate the overall connectivity of conductive networks in SSCCs, the frequency-dependent AC electrical resistance of SSCCs with CFs and with CF-CNTs as a function of filler content was measured. AC measurement can avoid electrical polarization through continuous electrical charging and discharging, thus reflecting the real electrical resistance characteristics of SSCCs [7]. As shown in Figure 6, AC electrical resistances of SSCCs with CFs and with CF-CNTs with different filler contents decreased with the increasing frequency, from 100 Hz to 100 kHz. This can be attributed to lower capacitances in SSCCs at higher test frequencies, thus lower electrical resistances [76]. For SSCCs with CFs (Figure 6c), the specimens exhibited similar percolation behavior to DC electrical resistance measurements. In contrast, the SSCCs with CF-CNTs showed an apparent percolation zone ranging from 0.5 vol.% to 1.5 vol.%, in which the AC electrical resistances of the SSCCs with CF-CNTs decreased sharply (Figure 6d). For CF-CNT contents above 1.5 vol.%, the AC electrical resistance remained almost unchanged. In particular, the AC electrical resistance of SSCCs with 5 vol.% CF-CNTs became nearly constant as the frequency increased, suggesting an entire conductive network formed in SSCCs as verified by the BSE characterization (Figure 6d, inset). This further verifies the result of DC electrical resistance measurements that CF-CNTs were more effective conductive fillers than CFs in terms of enhancing the conductivity of SSCCs.

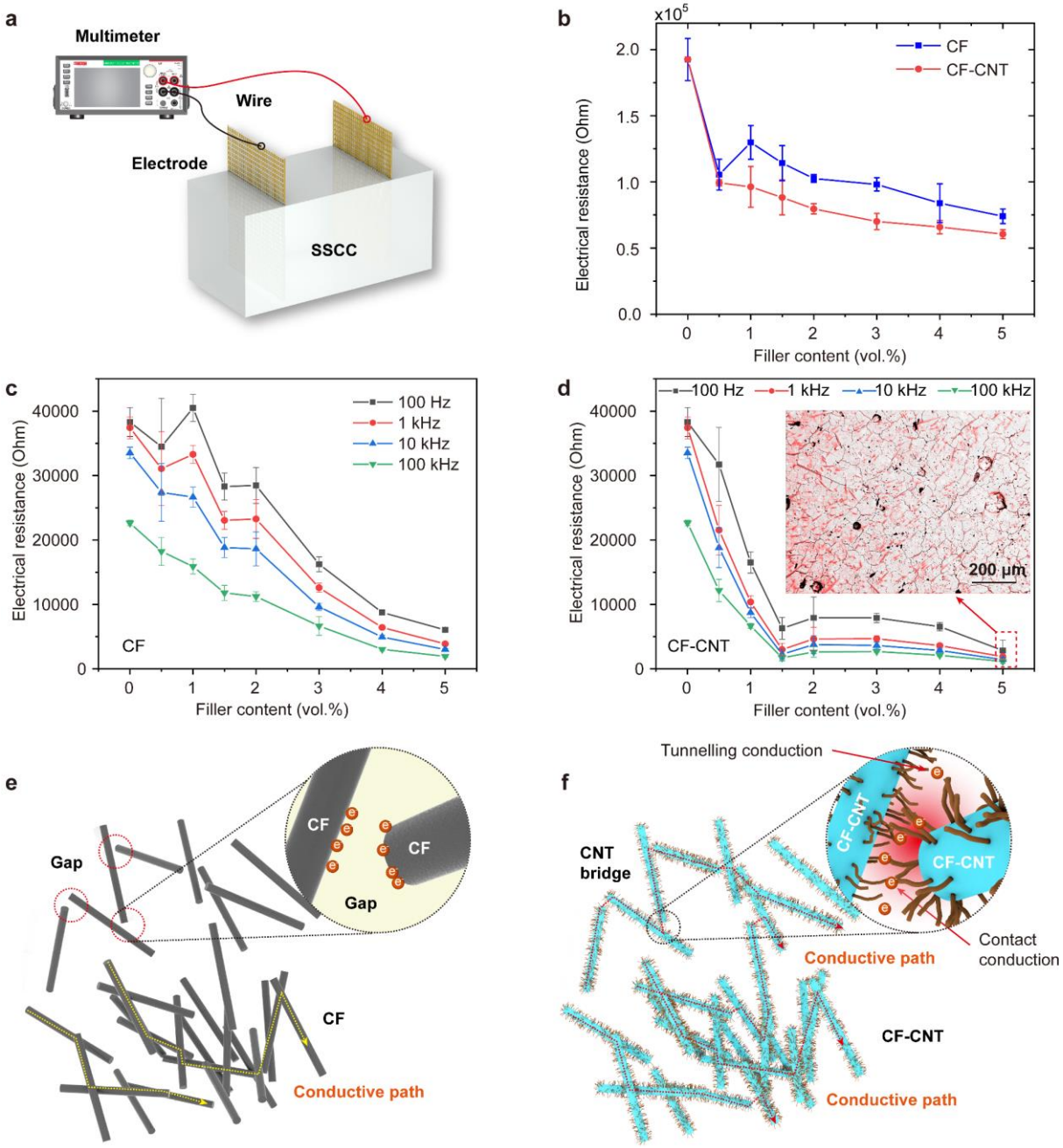


**Figure 6.** Electrical properties of SSCCs with CF-CNTs. (a) Schematic illustration of two-probe electrical resistance measurement. (b) DC electrical resistance of the SSCCs with CFs and with CF-CNTs as a function of filler content after curing 28 days. AC electrical resistance of the SSCCs with (c) CFs and (d) CF-CNTs as a function of filler content after curing 28 days. (Inset shows the BSE image of the SSCC with 5 vol.% CF-CNTs, CF-CNTs were marked in red). Illustration of conductive mechanism of SSCCs with (e) CFs and (f) CF-CNTs.

The enhanced conductivity of SSCCs with CF-CNTs can be explained as follows. As individual CFs are randomly dispersed in SSCCs with CFs alone, only a few conductive paths

can be formed via CF contact conduction when the filler content is below the percolation threshold (Figure 6e). However, in the case of the SSCCs with CF-CNTs, on one hand, the inherently superior conductivity of CNTs can improve the bulk conductivity of CF-CNTs. At the same time, CNTs grown on CF surfaces bridge between CFs to generate more conductive pathways for electron transportation via direct contact or tunnelling conduction, resulting in the formation of massive multiscale conductive networks throughout the matrix, i.e., CFs for long-scale conduction and CNTs for short-scale conduction (Figure 6f).

### 2.4. Self-sensing properties of SSCCs with CF-CNTs

Due to the excellent conductive nature of CF-CNT, it is envisioned as an effective filler to endow SSCCs with self-sensing properties. The self-sensing properties of SSCCs were performed as illustrated in **Figure 7**a. Under monotonically uniaxial compression, the fractional change in electrical resistance (FCR) of all SSCCs with CFs (Figure 7b) and with CF-CNTs (Figure 7c) decreased with increasing compressive stress, indicating their negative piezoresistivity. The FCR changed suddenly when the ultimate compressive strain was reached, indicating that SSCCs can be effectively functioned for structural health monitoring applications. More obvious evidence can be found in the FCR/strain/stress plots (Figure S8 and Figure S9) that a good agreement between the variation of electrical resistance and compressive stress/strain/crack/damage can be observed. The stress sensitivities ($FCR/\sigma$, where $\sigma$ is compressive strain) and gauge factors ($FCR/\varepsilon$, where $\varepsilon$ is compressive strain) of the two batches of SSCCs were highly dependent on the filler content and filler type (Figure S10). The maximum stress/strain sensitivities showed maxima at 1.5 vol.% CFs and 1.5 vol.% CF-CNTs, at values of 0.506% $MPa^{-1}$/175.1 and 0.506% $MPa^{-1}$/221.6, which are dozens of times higher than the blank specimen (0.0134 %/MPa/2.78). This indicates that the percolation thresholds of the SSCCs with CFs and with CF-CNTs were both 1.5 vol.%, verifying the fact that SSCCs with a filler content near the percolation threshold undergo an abrupt change of electrical resistance upon deformation, i.e., a high sensitivity.[7] In addition, except for the filler content of 1.5 vol.%, the SSCCs with CF-CNTs always had lower stress sensitivities and gauge factors than the SSCCs with CFs at the same filler content. However, the responses of SSCCs with CF-CNTs to uniaxial compression demonstrated better smoothness and higher linearity in comparison to SSCCs with CFs. These results suggest that SSCCs with CF-CNTs were less sensitive but more stable than SSCCs with CFs, which may be attributed to the enhanced fiber/cement matrix interfacial interaction of CF-CNTs

restricting fiber push-in and reorientation, resulting in lower sensitivity. The higher stability arises because the gaps between CFs were effectively bridged by CNTs, ensuring effective conduction paths during cyclic loading via more uniform hierarchical and stable conductive networks.[36,37,77,78] However, due to the more obvious percolation phenomenon observed in the case of SSCCs with CF-CNTs (Figure 6), SSCCs with 1.5 vol.% CF-CNTs demonstrated the highest sensitivity.

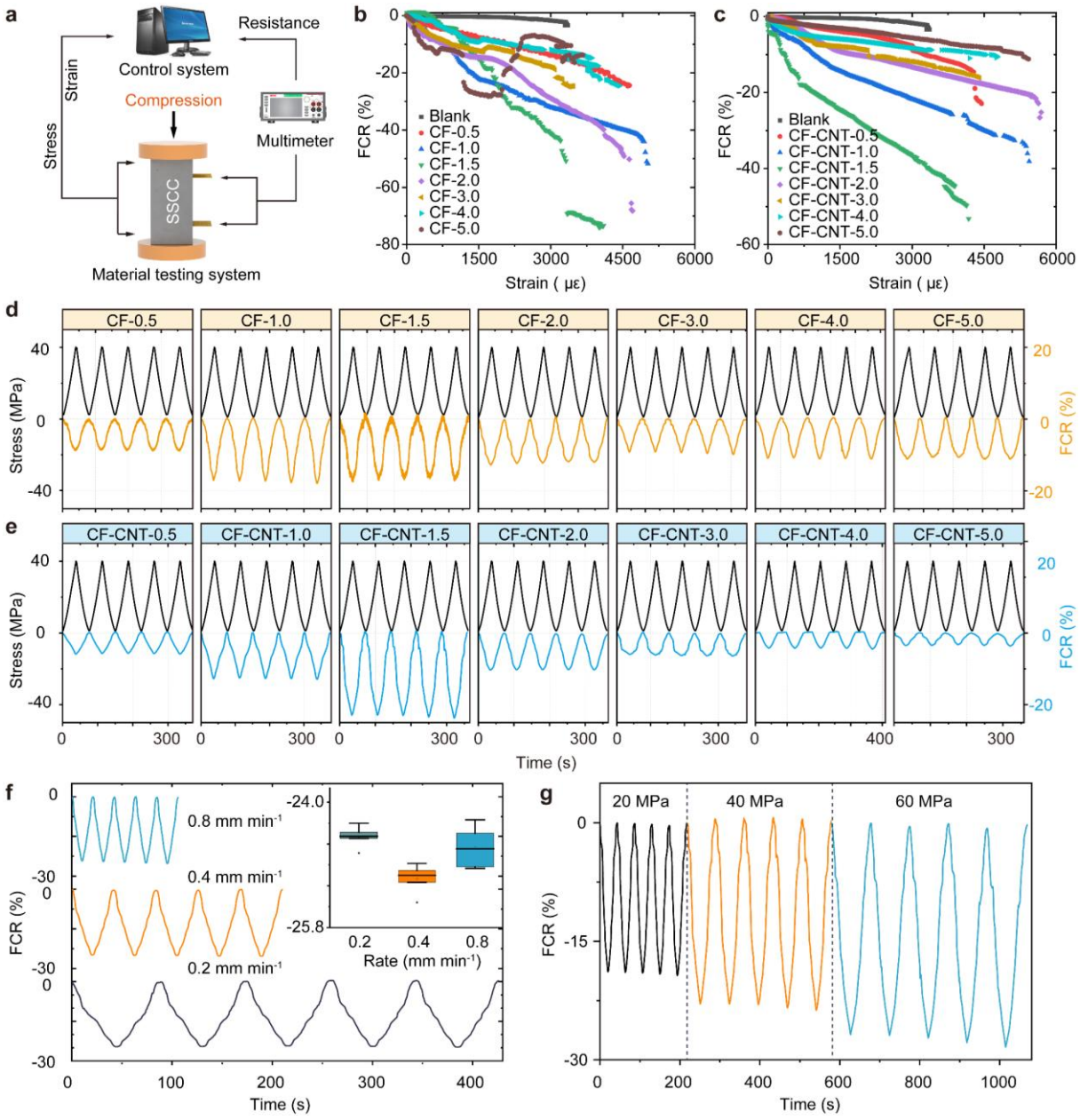


**Figure 7.** Self-sensing properties of SSCCs. (a) Illustration of self-sensing properties measurement. (b) FCR *versus* Strain for SSCCs with CFs. (c) FCR *versus* Strain for SSCCs with CF-CNTs. (d) Self-sensing properties of the SSCCs with CFs under cyclic compression with a loading rate of 0.4 mm $min^{-1}$ and a stress amplitude of 40 MPa. (e) Self-sensing

properties of the SSCCs with CFs under cyclic compression with a loading rate of 0.4 mm $min^{-1}$ and a stress amplitude of 40 MPa. (f) Self-sensing properties of the SSCCs with 1.5 vol.% CF-CNTs under different loading rates, with a stress amplitude of 40 MPa. (g) Self-sensing properties of the SSCCs with 1.5 vol.% CF-CNTs under different loading amplitudes, with a loading rate of 0.4 mm $min^{-1}$.

Furthermore, the stability and repeatability of SSCCs were evaluated under 5 cycles of repetitive compression with an amplitude of 40 MPa and a loading rate of 0.4 mm $min^{-1}$ (Figure 7c, e). Under cyclic compression, the FCR of all SSCCs steadily increased upon compression and then symmetrically decreased during unloading in each cycle. At the same time, the FCR of the control still demonstrated a sustained decay over time due to the remaining polarization influence, except for the blank specimen whose FCR demonstrated a sustained upward trend due to severe polarization. In addition, the maximum stress sensitivity was observed in the case of the SSCCs with 1.5 vol.% CF-CNTs, consistent with the results of monotonic compression. The excellent self-sensing performance indicates the uniform dispersion of CF-CNTs in the composites.[79–81] The repeatability of SSCCs was further investigated under cyclic compressive loadings with loading rates (0.2 mm $min^{-1}$, 0.4 mm $min^{-1}$, and 0.8 mm $min^{-1}$ under 40 MPa, Figure 7f) and different stress amplitudes (20 MPa, 40 MPa, and 60 MPa at 0.4 mm $min^{-1}$, Figure 7g). For the sake of simplicity, only the SSCC with 1.5 vol.% CF-CNTs was chosen due to its highest sensitivity. The SSCCs with 1.5 vol.% CF-CNTs sample demonstrated stable and consistent cyclic responses and outstanding adaptability to various applied conditions, as evidenced by the constant maximum FCR value in each cycle. It is therefore concluded that the CF-CNT, as a new type of functional filler, has great potential in the fabrication of SSCCs with the advantages of high mechanical properties, tailored design, high sensitivity, and excellent robustness, offering a forward step towards the up-scaling deployment of SSCCs for structural health monitoring.

### 2.5. Application of SSCCs with CF-CNTs for crack development monitoring of maglev girder

Benefiting from the good mechanical properties, excellent self-sensing performance, and favorable compatibility with concrete structures, the as-fabricated SSCCs with CF-CNTs could be potentially applied for real-time and in-situ structural health monitoring. Here, we integrated the SSCCs with 1.5 vol% CF-CNTs into a full-scale maglev girder used for a real

medium-low speed maglev transportation project in Qingyuan, China, aiming at developing a smart maglev girder monitoring system, and presented a preliminary study for monitoring crack development of the maglev girder under static load test (**Figure 8**a). Two SSCCs named S1 and S2 were perpendicularly deployed at the midspan and the support of the maglev girder respectively, 15 mm away from the concrete surface and fixed on the reinforcing bars using plastic ribbon and insulation tape. As shown in Figure 8b, the maglev girder was loaded by ten pairs of hydraulic jacks, uniformly placed on the top surface, and was simply supported with a span of 24.2 m. In order to confirm the embedment positions of SSCCs, the stress conditions of the maglev girder after prestress tension and at different static loading stages were analyzed by using finite element (FE) simulations (detailed simulation method is available in the Supplementary material, Figure S11, Figure S12, Table S4, and Table S5). Figure 8c shows that the maximum compressive stress of the maglev girder under static load test appears at the top side of the beam mid-span. The support is also stressed during static loading, with increased compressive stress with the increase of the static load. However, strain value at the support is dozens of times smaller than that at the midspan.

Figure 8d show the responses of two SSCCs, S1 and S2 during the whole loading procedure. It can be seen that the voltage variations of the two SSCCs exhibited great correlations with the time history of the applied load. As the load increased, the SSCCs inside the maglev girder were compressed, resulting in a reduction in their electrical resistances and an increase in voltage variations. Note that minor peaks were observed in each loading instant due to the disturbance of hydraulic jack vibration. As expected, more significant voltage variations were observed for S1 at the midspan than S2 at the support, which is in agreement with the FE results that the internal stress at the midspan is much larger than that at the support, indicating the high fidelity of SSCCs' performance. Importantly, the electrical signals of both SSCCs were suddenly increased at a load of 249 kN, marking the first major crack appearance. Afterward, as the applied load increased, the electrical signals fluctuated with obvious noises, indicating the propagation and evolution of multi-cracks in the maglev girder, as evidenced by a good correlation between the electrical signals and the crack pattern (Figure 8e) recorded during the experiment. The maximum voltage variations both occurred at the ultimate load (414 kN), at which another major jump of electrical signal corresponding to the structure failure was observed. More importantly, voltage variations decreased during the unloading process and almost recovered to the initial state, indicating the structure and function integrity of the two SSCCs during the whole destruction process of the maglev girder, even after

complete failure. This phenomenon benefited from the improved mechanical properties with the incorporation of CF-CNT, which would allow the long-term non-destructive monitoring of a wide variety of concrete structures with different strength levels. Therefore, the developed system is suitable to capture the initiation of crack/damage, as well as progressive and sudden damage events until complete failure, but fails to provide information about the width/size/degree of damage.

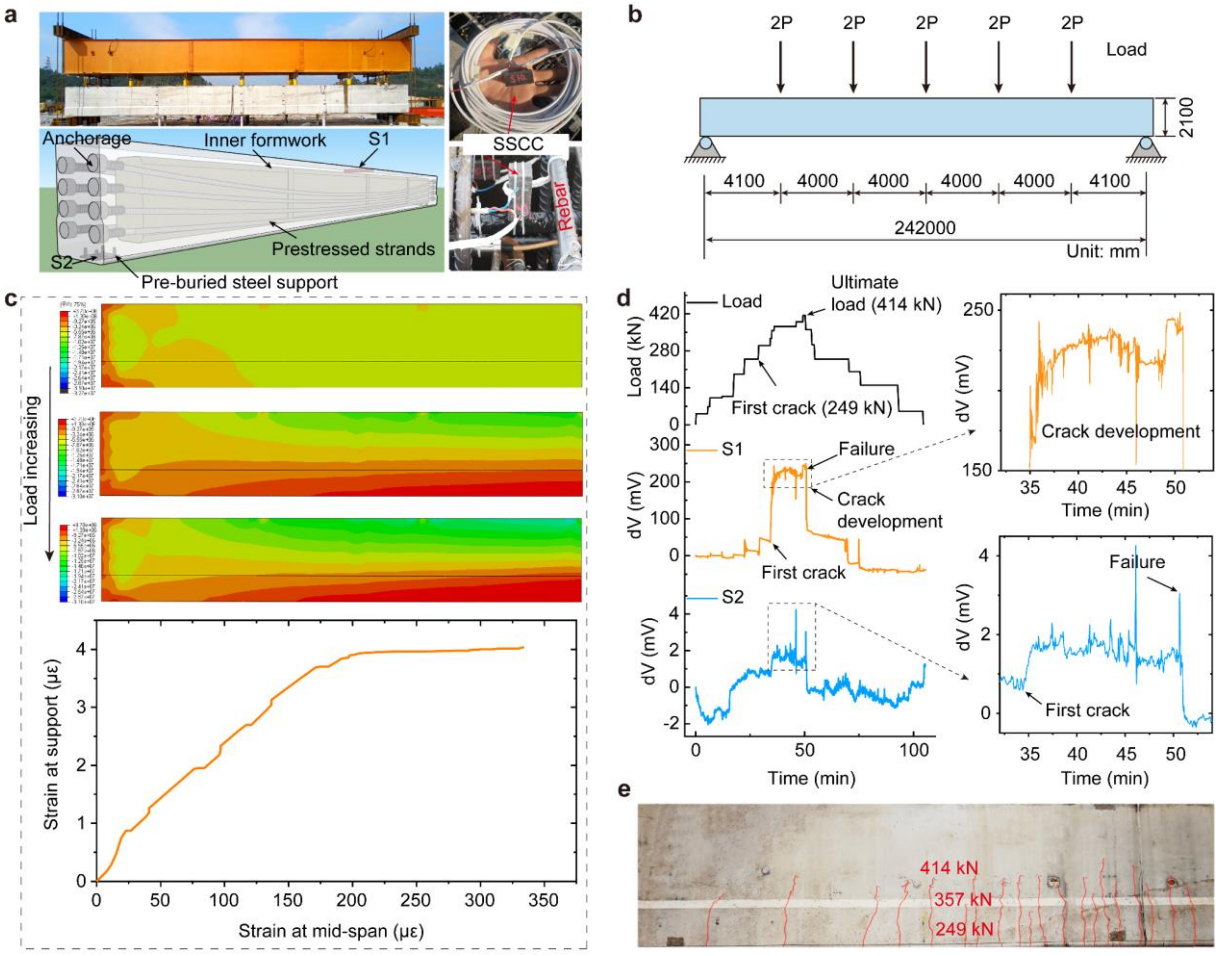


**Figure 8.** Application of the SSCCs for crack monitoring. (a) Schematic diagram and photograph of smart maglev girder configuration and sensor deployment. (b) Loading procedure. (c) Finite element analysis of longitudinal stress distribution in smart maglev girder concrete during loading and comparison of strains at support and midspan. (d) Sensing signals of S1 and S2 during loading. (e) Crack pattern after ultimate load.

## 3. Conclusion

In summary, we reported a new-generation of SSCCs comprising hierarchically structured functional filler, CF-CNT, for the purpose of alleviating the CNT's dispersion problem and enable scalable manufacturing of SSCCs with outstanding self-sensing performance and enhanced mechanical properties. The hierarchically structured CF-CNT composite filler was in-situ CVD synthesized by directly growing CNTs on CFs. High loadings of oriented CNTs with a radial arrangement was successfully deposited on CFs' surface, which leads to an enhanced BET specific surface area, thus providing a stronger interfacial bonding between CF-CNTs and cement matrix. By assembling CF-CNT hierarchical fillers within cement matrix, SSCCs exhibited impressive mechanical properties relative to the blank specimen. SEM observation revealed that CF-CNT can effectively enhance fiber/cement matrix interfacial bond strength by encouraging part of hydration products penetrating CNT forests, filling in porous structures surrounding CFs to improve the ITZ microstructure, bridging the nano-scale cracks and transferring load from CF to itself. However, due to the performance degradation of CF, exfoliation of CNT agglomerations as well as the dilution effect of the high mass fraction of CNTs in the CF-CNT, the flexural properties of SSCCs with CF-CNTs were not comparable to SSCCs with CFs. CF-CNTs were more effective conductive fillers than CFs in terms of the enhancement of SSCC conductivity. Due to the enhanced filler/matrix interfacial interactions and the synergic and spatially morphological effects of CF-CNT, the SSCCs with 1.5 vol.% CF-CNTs achieved a maximum stress/strain sensitivity of 0.638% $MPa^{-1}$/221.6 and better smoothness and higher linearity in comparison to SSCCs with CFs. The as-fabricated SSCCs with CF-CNTs were successfully applied for monitoring crack development of a maglev girder under static load, indicating its broad application prospects in structural health monitoring and facilitating low-carbon, high-performance, multifunctional, and sustainable development of civil infrastructures. Future work will focus on the application of low-temperature plasma-enhanced or photo-thermal CVD method or the application of barrier coatings on CF surface that allows the growth of CNTs with minimum thermally-induced degradation to the underlying CFs, and the performance modulation of SSCCs with CF-CNT synthesized under different CVD regimes and catalysts to identify how the hierarchical structures' morphologies (i.e., length, diameter, and density) produced affect the resultant SSCC's performance.

## 4. Experimental Section

*Synthesis of CF-CNTs via in-situ CVD method*: Unsized polyacrylonitrile (PAN)-based short-cut CFs (approximately 2 mm in length, 7 μm in diameter, T700S-12K, Toray, Japan) were

used throughout this work. Nickel nitrate hexahydrate ($Ni(NO_3)_2 \cdot 6H_2O$, 99%, 100 mM, Acros) and iron nitrate hexahydrate ($Fe(NO_3)_3 \cdot 9H_2O$, 99%, 100 mM, Sigma-Aldrich) were used as catalysts and diluted with isopropanol ($C_3H_8O$, 99.6%, Acros). First, the as-obtained CFs were ultrasonically (45 kHz, 120 W, Crest) cleaned in isopropanol for 2 h and then in ultrapure water (18 MΩ cm, Barnstead Smart2Pure, USA) for 1 h. After being dried at 105 ºC for 4 h, CFs were ultrasonically treated with $HNO_3$ (65%, Acros) for 2 h, followed by several water washes until neutralization. For the catalyst impregnation, the oxidized CFs were immersed into the catalyst precursor isopropanol solution for 2 h along with the assistance of ultrasonic treatment (45 kHz, 120 W). Subsequently, the catalyst pre-deposited CFs were filtered from the solution and oven-dried at 80 ºC for 24 h. The growth of CNTs was performed in an ambient pressure CVD system (approximately 60 mm in diameter, OTF-1200X, MTI Co., Ltd.) using acetylene ($C_2H_2$, 99.9%) as carbon source. Prior to the reactions, the CVD system was initially purged with a $N_2$ (500 sccm, 99.999%) flow to displace the oxygen. To improve the catalytic activity, an additional H2 (20 sccm, 99.999%) flow was introduced at 400 ºC as reductant for 20 min. Then, the CVD system was heated at a rate of 10 ºC $min^{-1}$ to the desired temperatures (450 ºC- 850 ºC) under a gas mixture of $C_2H_2/H_2/N_2$ for different growth times. The tube was then allowed to cool down to room temperature under $N_2$ flow (100 sccm).

*Preparation of SSCCs with CF-CNTs:* The raw materials used for the preparation of SSCC specimens mainly include pristine CFs, as-synthesized CF-CNTs, cement (P.O. 42.5R, Dalian Onoda Cement Co. Ltd., China), silica fume (920D, Shanghai Tian Kai Silicon Fume Co. Ltd., China), tap water and polycarboxylate-based superplasticizer (ViscoCrete 3301E, Sika Ltd., China). The preparation process of SSCC specimens was as follows: (1) low-speed dry-mixing of the pre-weighed CF-CNTs with silica fume using a mechanical stirrer (MXF-C, Shanghai Muxuan Industrial Co., Ltd.) for 2 min; (2) mixing the polycarboxylate superplasticizer with water and adding the solution into the mixture, with a 30 s of low-speed stirring; (3) adding cement to the suspension slowly in three divided portions with low-speed stirring firstly for 30 s followed by a 2-min high-speed stirring; (4) pouring the well-stirred mixture into moulds and embedding two copper electrodes with an interval of 20 mm for compression samples and 60 mm for flexural samples; (5) vibrating the moulds on an electric vibrator to eliminate bubbles; (6) curing the specimens in a standard curing box and demoulding after 24 h; (7) curing the specimens in a lime-saturated tank at room temperature

for 27 days. In this study, the compression specimens were 20 × 20 × 40 $mm^3$, and the flexural specimens were 20 × 20 × 80 $mm^3$.

*Morphology and structure characterization of CF-CNTs and SSCCs with CF-CNTs:* Field emission scanning electron microscopy (FESEM, Hitachi SU8020, Japan) at an operating voltage of 5 kV and transmission electron microscope (JEOL 2100F, Japan) at an operating voltage of 200 kV was used to characterize the morphologies of CF-CNT. The crystalline structure of CF-CNT was determined by X-ray diffraction (XRD) measurement (PANalytical X'Pert PRO MPD, Netherlands) with CuKα radiation. XRD patterns were collected in the 2θ range of 10-80° with a step width of 0.02° and a step time of 1.0 s. Raman spectra were collected in a Raman spectroscopy (Renishaw inVia plus, Britain) under ambient conditions with an excitation laser wavelength of 532 nm, with a resolution of 2 $cm^{-1}$ in the range of 800 to 2000 $cm^{-1}$. The Brunauer-Emmett-Teller (BET, Micromeritics Tristar ASAP 2020HD88, USA) specific surface area of CF-CNT was measured by $N_2$ adsorption measurements at about 77 K. Thermogravimetric analysis (TGA, Mettler Toledo TGA/DSC1, Switzerland) were conducted under air atmosphere (23% oxygen) with a temperature ramp of 5 ºC $min^{-1}$ from 20-900 ºC. The weight fraction of CNTs in the CF-CNTs ($\omega_{CNT}$, wt%) is estimated by:

$$\omega_{CNT} = A_{CNT}/A_{CF\text{-}CNT} \quad (1)$$

where $A_{CNT}$ is peak area corresponding to the weight loss of CNT in the DTG curve of the CF-CNT sample; $A_{CF\text{-}CNT}$ is total peak area in the DTG curve of the CF-CNT sample. Each peak area was calculated using the Peak Analyzer tool in OriginPro 2022b.

For the characterization of SSCCs, the hydration of the finely ground samples was stopped by solvent exchange using isopropanol and then in acetone for 20 s. Afterward, the samples were washed with isopropanol and stored in a vacuum desiccator until further testing. TGA measurements with a heating rate of 10 ºC $min^{-1}$ up to 1000 ºC under $N_2$ atmosphere and XRD measurements with the same setting for CF-CNTs were performed. The microstructure of SSCC with CF-CNT specimens after fracture was observed using a FESEM (Tescan MAIA3, Czech). For backscattered electron imaging observation (BSE, Tescan VEGA3, Czech), the fractured samples were encapsulated in epoxy resin (EpoThin2, Buehler, USA ) and polished using an automatic polishing machine (AutoMet 300, Buehler, USA) by successive polishing for 3 min with a grit 600 abrasive paper under a force of 3 lbs, followed by 5 min with a 9 μm MetaDi supreme diamond suspension at 5 lbs, 10 min with a 3 μm MetaDi supreme diamond suspension at 5 lbs, and 30 min with a 0.05 μm MasterPrep

alumina suspension at 3 lbs. Between each step, the samples were ultrasonically cleaned in isopropanol for 5 min to remove the residual polishing agent on the sample surface. Energy-dispersive X-ray spectroscopy (EDS) analysis was performed to determine the element distribution in the SSCC samples, using the Aztec software at a resolution of 1024 × 768 pixels with a 200 μs dwell time per pixel and 3 frames per scan.

*Tests of mechanical, electrical and self-sensing properties of SSCCs with CF-CNTs:* The flexural strength of SSCC specimens with dimensions of 20 × 20 × 80 $mm^3$ was measured using an Instron 5567A universal mechanical testing machine (Instron Inc., Norwood, MA, USA) at a constant loading rate of 0.02 mm $min^{-1}$. The distance between the two supports was fixed at 60 mm. The compressive strength of SSCC specimens with dimension of 20 × 20 × 40 $mm^3$ was tested using a hydraulic material testing system (WDW-200E, Jinan Time Assay Machine Co., Ltd., China) with a constant loading rate of 1.2 mm $min^{-1}$. Two longitudinal strain gauges were symmetrically deployed on a pair of opposite sides of each specimen, and a dynamic data logger (DC-204R, TML, Japan) was used for strain measurements. The flexural and compressive strengths of SSCCs were, both, taken as the average of three specimens. As to the electrical properties of SSCCs, the direct current (DC) electrical resistance of the unloaded SSCCs was measured by a two-probe method using a digital multimeter (DMM7510, Keithley Instruments Inc., USA). The two-electrode alternating current (AC) electrical resistance of the SSCCs was measured using a LCR meter (U1733C, Agilent Technologies Inc., USA). Each specimen's electrical resistance was calculated by taking the average of three data collected after 2 h to mitigate any shift due to the polarization effect. The self-sensing properties of SSCCs were performed on 20 × 20 × 40 $mm^3$ specimens, under repeated cycles of compression with different loading rates and amplitudes using the WDW-200E machine. Two longitudinal strain gauges symmetrically attached parallel to the loading direction were used to measure compressive strain. Prior to the tests, all samples were connected to the ends of the multimeter for 2 h to minimize the polarization effect on resistance variations. During the loading process, the compressive force, strain and electrical resistance were simultaneously collected at a sampling rate of 10 Hz. The specimens were separated from the compression platens by thin insulting plates to avoid electrical interference. All experiments were conducted at room temperature. FCR was calculated as:

$$FCR = \Delta R/R_0 = (R_t - R_0)/R_0 \quad (2)$$

where $\Delta R$ is the change in electrical resistance, $R_0$ and $R_t$ are measured electrical resistances prior to loading and at time $t$, respectively.

*Tests of smart maglev girder assembly and crack sensing capacity:* The prepared SSCCs were integrated into a full-scale maglev girder to test the crack sensing capacity. The maglev girder used was a prestressed simply-supported box girder (C50 ready-mixed concrete, 25 m long, 2.1 m tall, 1.3 m top wide and 1.4 m bottom wide), in which 8 prestressed steel strands were preset to achieve a prestressed tension of 1270 MPa. For static loading test, a concentrated force was synchronously applied on ten steel plates placed the top surface of the maglev girder by ten hydraulic jacks with a loading speed of 3 kN $s^{-1}$. The steel plate with a dimension of 400 × 400 × 27 $mm^3$ was symmetrically arranged with a longitudinal spacing of 4 m and a transverse spacing of 1 m. The electrical resistance change of SSCCs was converted into a voltage signal by connecting the sensor with a reference resistor (1000 Ω) for voltage sharing. The voltage signal was collected using a data acquisition system (DH-3820, Donghua Analysis Instruments Co., Ltd, China) and a computer with a sampling rate of 1 kHz via shielded wires. The numerical simulations were conducted in a commercial platform, Abaqus CAE 6.

**Supporting Information**

Supporting Information is available from the Wiley Online Library or from the author.

**Acknowledgements**

The work described in this paper is supported by grants from the National Science Foundation of China (51978127 and 51578110) and grants from the China Postdoctoral Science Foundation (2022M710973 and 2022M720648).

**Conflict of Interest**

The authors declare no conflict of interest.

**Data Availability Statement**

The data that support the findings of this study are available from the corresponding author upon reasonable request.

Received: ((will be filled in by the editorial staff))
Revised: ((will be filled in by the editorial staff))
Published online: ((will be filled in by the editorial staff))

References

[1] J. Su, Y. Xia, S. Weng, *Struct. Control. Health Monit.* **2020**, *27*, e2629.

[2] Q. Zhang, K. Barri, S. R. Kari, Z. L. Wang, A. H. Alavi, *Adv. Funct. Mater.* **2021**, *31*, 2105825.

[3] A. Mirabedini, A. Ang, M. Nikzad, B. Fox, K. Lau, N. Hameed, *Adv. Sci.* **2020**, *7*, 1903501.

[4] H. Im, S. Hong, Y. Lee, H. Lee, S. Kim, *Adv. Mater.* **2019**, *31*, 1807552.

[5] Y. Ni, Y. Xia, W. Liao, J. Ko, *Struct. Control. Health Monit.* **2009**, *16*, 73.

[6] S. Ding, S. Dong, A. Ashour, B. Han, *J. Appl. Phys.* **2019**, *126*, 241101.

[7] B. Han, S. Ding, X. Yu, *Measurement* **2015**, *59*, 110.

[8] D. Dimov, I. Amit, O. Gorrie, M. Barnes, N. Townsend, A. Neves, F. Withers, S. Russo, M. Craciun, *Adv. Funct. Mater.* **2018**, *28*.

[9] M. Krystek, A. Ciesielski, P. Samorì, *Adv. Funct. Mater.* **2021**, *31*, 2101887.

[10] M. Islam, S. Afroj, M. Uddin, D. Andreeva, K. Novoselov, N. Karim, *Adv. Funct. Mater.* **2022**, 2205723.

[11] F. Ubertini, S. Laflamme, H. Ceylan, A. Luigi Materazzi, G. Cerni, H. Saleem, A. D'Alessandro, A. Corradini, *Smart Mater. Struct.* **2014**, *23*, 45023.

[12] E. García-Macías, F. Ubertini, *Earthq. Eng. Struct. Dyn.* **2019**, *48*, 548.

[13] S. Ding, Y. Wang, Y. Ni, B. Han, *Smart Mater. Struct.* **2020**, *29*, 055013.

[14] R. Howser, H. Dhonde, Y. Mo, *Smart Mater. Struct.* **2011**, *20*, 85031.

[15] M. Tafesse, A. Alemu, H. Lee, C. Cho, H. Kim, *Cem. Concr. Compos.* **2022**, *133*, 104662.

[16] S. Ding, Y. Xiang, Y. Ni, V. Thakur, X. Wang, B. Han, J. Ou, *Nano Today* **2022**, *43*, 101438.

[17] P. Chen, D. Chung, S. Materials, *Smart Mater. Struct.* **1993**, *2*, 22.

[18] B. Chen, J. Liu, K. Wu, *Cem. Concr. Res.* **2005**, *35*, 2183.

[19] B. Han, X. Guan, J. Ou, *Sens. Actuator A-Phys.* **2007**, *135*, 360.

[20] J. Xu, T. Yin, Y. Wang, L. Liu, *Cem. Concr. Compos.* **2021**, *116*, 103873.

[21] B. Han, X. Yu, J. Ou, *Self-Sensing Concrete in Smart Structures*, Elsevier, Netherlands, **2014**.

[22] A. Belli, A. Mobili, T. Bellezze, F. Tittarelli, *Cem. Concr. Compos.* **2020**, *109*, 103569.

[23] L. Wang, F. Aslani, *Ceram. Int.* **2021**, *47*, 7864.

[24] X. Fu, W. Lu, D. Chung, *Carbon* **1998**, *36*, 1337.

[25] L. Lavagna, S. Musso, G. Ferro, M. Pavese, *Cem. Concr. Compos.* **2018**, *88*, 165.

[26] P. Garcés, J. Fraile, E. Vilaplana-Ortego, D. Cazorla-Amorós, E. G. Alcocel, L. G. Andión, *Cem. Concr. Res.* **2005**, *35*, 324.

[27] X. Xi, D. D. L. Chung, *Carbon* **2019**, *145*, 401.

[28] H. Li, M. Liebscher, I. Curosu, S. Choudhury, S. Hempel, M. Davoodabadi, T. T. Dinh, J. Yang, V. Mechtcherine, *Cem. Concr. Compos.* **2020**, *114*, 103777.

[29] F. Yang, S. Qian, *Constr. Build. Mater.* **2020**, *260*, 119717.

[30] W. Qin, F. Vautard, L. Drzal, J. Yu, *Compos. Pt. B-Eng.* **2015**, *69*, 335.

[31] A. Dehghani, F. Aslani, *Constr. Build. Mater.* **2020**, *120*, 121046.

[32] Y. Ding, Z. Han, Y. Zhang, J. Aguiar, *Compos. Struct.* **2016**, *138*, 184.

[33] B. Han, J. Ou, *Sensor. Actuat. A- Phys.* **2007**, *138*, 294.

[34] B. Chen, B. Li, Y. Gao, T. Ling, Z. Lu, Z. Li, *Constr. Build. Mater.* **2017**, *144*, 106.

[35] S. Taheri, J. Georgaklis, M. Ams, S. Patabendigedara, A. Belford, S. Wu, *J. Mater. Sci.* **2022**, *57*, 2667.

[36] G. Kim, S. Park, G. Ryu, H. Lee, *Cem. Concr. Compos.* **2017**, *82*, 165.

[37] F. Azhari, N. Banthia, *Cem. Concr. Compos.* **2012**, *34*, 866.

[38] D. Lu, D. Wang, J. Zhong, *Cem. Concr. Compos.* **2022**, *134*, 104731.

[39] M. De Volder, S. Tawfick, R. Baughman, A. Hart, *Science* **2013**, *339*, 535.

[40] I. Kinloch, J. Suhr, J. Lou, R. Young, P. Ajayan, *Science* **2018**, *362*, 547.

[41] A. Sobolkina, V. Mechtcherine, V. Khavrus, D. Maier, M. Mende, M. Ritschel, A. Leonhardt, *Cem. Concr. Compos.* **2012**, *34*, 1104.

[42] S. Parveen, S. Rana, R. Fangueiro, M. C. Paiva, *Cem. Concr. Res.* **2015**, *73*, 215.

[43] A. D'Alessandro, M. Rallini, F. Ubertini, A. L. Materazzi, J. M. Kenny, *Cem. Concr. Compos.* **2016**, *65*, 200.

[44] H. Qian, E. S. Greenhalgh, M. Shaffer, A. Bismarck, *J. Mater. Chem.* **2010**, *20*, 4751.

[45] X. Liu, Y. Song, C. Li, F. Wang, *Carbon* **2013**, *55*, 377.

[46] F. Zhao, Y. Huang, L. Liu, Y. Bai, L. Xu, *Carbon* **2011**, *49*, 2624.

[47] H. Qian, A. Bismarck, E. S. Greenhalgh, G. Kalinka, M. S. P. Shaffer, *Chem. Mat.* **2008**, *20*, 1862.

[48] C. He, N. Zhao, C. Shi, E. Liu, J. Li, *Adv. Mater.* **2015**, *27*, 5422.

[49] Q. Zhang, J. Q. Huang, M. Q. Zhao, W. Z. Qian, F. Wei, *ChemSusChem* **2011**, *4*, 864.

[50] T. Pozegic, I. Hamerton, J. Anguita, W. Tang, P. Ballocchi, P. Jenkins, S. Silva, *Carbon* **2014**, *74*, 319.

[51] V. Veedu, A. Cao, X. Li, K. Ma, C. Soldano, S. Kar, P. Ajayan, M. Ghasemi-Nejhad, *Nat. Mater.* **2006**, *5*, 457.

[52] J. Wang, L. Liu, S. Jiao, K. Ma, J. Lv, J. Yang, *Adv. Funct. Mater.* **2020**, *30*, 2002595.

[53] W. Fan, Y. Wang, C. Wang, J. Chen, Q. Wang, Y. Yuan, F. Niu, *Appl. Surf. Sci.* **2016**, *364*, 539.

[54] M. Anna, G. N. Albert, I. K. Esko, *J. Phys.-Condes. Matter* **2003**, *15*, S3011.

[55] C. Cheung, A. Kurtz, H. Park, C. Lieber, *J. Phys. Chem. B* **2002**, *106*, 2429.

[56] D. Yoo, S. Kang, J. Lee, Y. Yoon, *Cem. Concr. Res.* **2013**, *54*, 180.

[57] D. Yoo, B. Chun, J. Kim, *Cem. Concr. Res.* **2019**, *122*, 196.

[58] K. Kim, W. Yu, J. Youk, J. Lee, *ACS Appl. Mater. Interfaces* **2012**, *4*, 2250.

[59] S. Jiang, D. Zhou, L. Zhang, J. Ouyang, X. Yu, X. Cui, B. Han, *Arch. Civ. Mech. Eng.* **2018**, *18*, 60.

[60] G. Faneca, I. Segura, J. M. Torrents, A. Aguado, *Cem. Concr. Compos.* **2018**, *92*, 135.

[61] S. He, Z. Li, E. H. Yang, *Cem. Concr. Res.* **2019**, *122*, 136.

[62] H. Le, D. Moon, D. Kim, *Constr. Build. Mater.* **2018**, *170*, 129.

[63] X. Wang, S. Ding, L. Qiu, A. Ashour, Y. Wang, B. Han, J. Ou, *Compos. Pt. B-Eng.* **2022**, *239*, 109960.

[64] A. Chaipanich, T. Nochaiya, W. Wongkeo, P. Torkittikul, *Mater. Sci. Eng. A-Struct. Mater. Prop. Microstruct. Process.* **2010**, *527*, 1063.

[65] G. Li, P. Wang, X. Zhao, *Carbon* **2005**, *43*, 1239.

[66] R. Abu Al-Rub, A. Ashour, B. Tyson, *Constr. Build. Mater.* **2012**, *35*, 647.

[67] J. Makar, J. Margeson, J. Luh, *J. Am. Ceram. Soc.* **2009**, 92, 1303.

[68] S. He, J. Qiu, J. Li, E. Yang, *Cem. Concr. Res.* **2017**, *98*, 50.

[69] R. Boris, V. Antonovič, J. Kerienė, R. Stonys, *J. Therm. Anal. Calorim.* **2016**, *125*, 1061.

[70] M. Konsta-Gdoutos, Z. Metaxa, S. Shah, *Cem. Concr. Res.* **2010**, *40*, 1052.

[71] F. Sanchez, C. Ince, *Compos. Sci. Technol.* **2009**, *69*, 1310.

[72] P. Xie, P. Gu, J. J. Beaudoin, *J. Mater. Sci.* **1996**, *31*, 4093.

[73] F. Azhari, N. Banthia, *ACI Mater. J.* **2017**, *114*, 129.

[74] L. Zhang, S. Ding, L. Li, S. Dong, D. Wang, X. Yu, B. Han, *Compos. Pt. A-Appl. Sci. Manuf.* **2018**, *109*, 303.

[75] B. Marinho, M. Ghislandi, E. Tkalya, C. E. Koning, G. de With, *Powder Technol.* **2012**, *221*, 351.

[76] B. Han, K. Zhang, X. Yu, E. Kwon, J. Ou, *Cem. Concr. Compos.* **2012**, *34*, 794.

[77] W. Li, D. He, J. Bai, *Compos. Pt. A-Appl. Sci. Manuf.* **2013**, *54*, 28.

[78] L. Wang, X. Xu, J. Chen, W. Su, F. Zhang, A. Li, C. Li, C. Xu, Y. Sun, *ACS Nano* **2022**, *16*, 12645.

[79] G. Li, P. Wang, X. Zhao, *Cem. Concr. Compos.* **2007**, *29*, 377.

[80] B. Han, L. Zhang, S. Zeng, S. Dong, X. Yu, R. Yang, J. Ou, *Compos. Pt. A-Appl. Sci. Manuf.* **2017**, 95:100.

[81] H. Kim, I. Park, H. Lee, *Compos. Struct.* **2014**, *116*, 713.

**Table of content**

Siqi Ding, Xinyue Wang, Liangsheng Qiu, Yi-Qing Ni, Xufeng Dong, Yanbin Cui, Ashraf Ashour, Baoguo Han * and Jinping Ou

**Self-sensing cementitious composites with hierarchical carbon fiber-carbon nanotube composite fillers for crack development monitoring of a maglev girder**

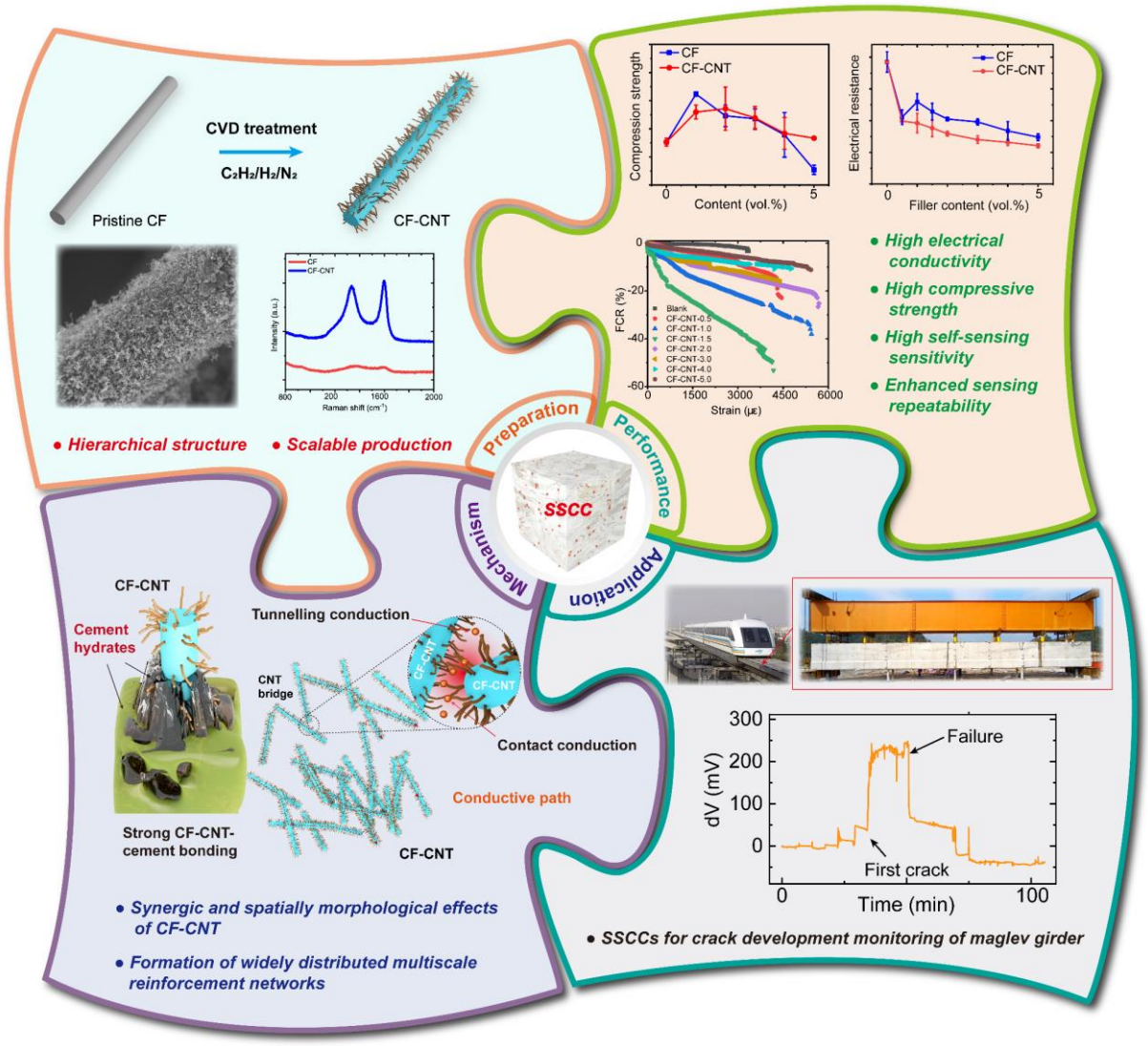


A new-generation SSCC incorporated with hierarchical CF-CNT composite filler exhibits impressive mechanical, electrical and self-sensing properties due to the widely distributed multiscale reinforcement networks caused by the synergic and spatially morphological effects of CF-CNT. Such SSCC can monitor crack development of a real maglev girder, thus providing the most fundamental materials for energizing sustainable infrastructures with in-situ monitoring capability.